

## Optimization of an electrokinetic mixer for microfluidic applications

Hendryk Bockelmann,<sup>1</sup> Vincent Heuveline,<sup>1</sup> and Dominik P. J. Barz<sup>2,a)</sup>

<sup>1</sup>*Engineering Mathematics and Computing Lab (EMCL), Karlsruhe Institute of Technology, Fritz-Erler-St. 23, D-76133 Karlsruhe, Germany*

<sup>2</sup>*Department of Chemical Engineering, Queen's University, Dupuis Hall 213, Kingston, Ontario K7L 3N6, Canada*

(Received 26 March 2012; accepted 9 May 2012; published online 24 May 2012)

This work is concerned with the investigation of the concentration fields in an electrokinetic micromixer and its optimization in order to achieve high mixing rates. The mixing concept is based on the combination of an alternating electrical excitation applied to a pressure-driven base flow in a meandering microchannel geometry. The electrical excitation induces a secondary electrokinetic velocity component, which results in a complex flow field within the meander bends. A mathematical model describing the physicochemical phenomena present within the micromixer is implemented in an in-house finite-element-method code. We first perform simulations comparable to experiments concerned with the investigation of the flow field in the bends. The comparison of the complex flow topology found in simulation and experiment reveals excellent agreement. Hence, the validated model and numerical schemes are employed for a numerical optimization of the micromixer performance. In detail, we optimize the secondary electrokinetic flow by finding the best electrical excitation parameters, i.e., frequency and amplitude, for a given waveform. Two optimized electrical excitations featuring a discrete and a continuous waveform are discussed with respect to characteristic time scales of our mixing problem. The results demonstrate that the micromixer is able to achieve high mixing degrees very rapidly.

© 2012 American Institute of Physics. [<http://dx.doi.org/10.1063/1.4722000>]

### I. INTRODUCTION

The field of microfluidics comprises the control and manipulation of flows with typical length scales in the range of micrometers and typical volumes in the range of nanoliters. Excellent reviews of such flows are available in Refs. 1–3. Several versatile technological concepts are based on microfluidics such as lab-on-a-chip (LOC) and micro reaction technology. The lab-on-a-chip concept is unique among microfluidic systems in that it aims for the integration of all unit operations that are required in a (bio-)chemical laboratory on one microfluidic chip of only few square centimeters in size. These steps typically include chemical synthesis or labeling of proteins, which require local mixing of reagents. Consequently, the investigation of mixing strategies in microfluidic devices is of particularly great interest. Mixing eventually occurs by diffusion on a molecular level and can, therefore, only be improved by two approaches: (i) via an enlargement of the (virtual) contact interfaces between the liquids/species to be mixed; and/or (ii) via decreasing of the molecular diffusion path. These features are usually achieved in macroscopic geometries by employing fluid-mechanical instabilities or turbulent flows. Contrary to flows in conventional channels, flows in microscopic channels are typically characterized by small Reynolds numbers in the range of  $Re \sim 0.01 - 10$ . At these low Reynolds numbers, inertial forces are weak and cannot be engaged to enhance mixing by flow instabilities or turbulence; other means are needed to facilitate mixing. A variety of microfluidic

---

<sup>a)</sup>dominik.barz@chee.queensu.ca.

mixing concepts has been proposed in literature. These concepts can principally be separated into two categories: (i) passive methods, which are based on suitable micro structures; (ii) active methods, which are associated with the introduction of energy into the system.

Many passive mixers take advantage of centrifugal or chaotic (secondary) flows, suitable to increase the contact interface of the liquids. Typical designs are T-mixers with different inlet channel diameters<sup>4</sup> or with J-shaped baffles in the common channel.<sup>5</sup> Other designs are based on meandering channels<sup>6</sup> combined with obstruction pillars,<sup>7</sup> perforations,<sup>8</sup> or baffles.<sup>9</sup> The so-called herringbone mixer is a very effective design for low Reynolds numbers using bas-relief structures on the channel floors.<sup>10,11</sup> Passive mixing can also be generated by taking advantage of viscoelastic flow instabilities whereas the applicability is limited to liquids with considerable viscosity difference.<sup>12</sup> Another passive mixer approach is the multi-lamination concept, i.e., the split-up of liquid streams into thinner lamellas and their subsequent recombination.<sup>13</sup> This concept is intended for both large contact areas and short diffusion paths without introducing a secondary flow. Generally, passive methods are linked to manufacturing of rather complex three-dimensional channel geometries and they often require relatively high Reynolds numbers.

Alternatively, active methods often allow for straightforward channel geometries, however, external forces have to be induced to create a secondary flow component. To date, several concepts have been realized based on different physicochemical phenomena. Ahmed *et al.*<sup>14</sup> demonstrate fast mixing inside a microfluidic channel due to the acoustic excitation of an air bubble trapped in a cavity. Khatavkar *et al.* propose a mixing concept based on an array of individually addressable artificial cilia covering the channel wall stirring the surrounding fluid.<sup>15</sup> Another concept by Yi *et al.* use magnetic forces to stir the liquids by applying a uniform magnetic field in conjunction with steady or time-dependent electrical currents.<sup>16</sup> Mixing as a result of simple low frequency vibration of the microfluidic device is reported by Oberti *et al.*<sup>17</sup> The vibrations induce vortices in proximity to sharp corners of the channel junctions.

Various lab-on-a-chip concepts rely on electrokinetic phenomena to realize unit operations, such as liquid pumping,<sup>18,19</sup> analyzing of ions,<sup>20</sup> or the manipulation of particles or cells.<sup>21–23</sup> Electrokinetic phenomena are related to the presence of an electrical double layer (EDL); comprehensive review is given in Ref. 24. Electroosmosis, also called electrokinetic flow, is the motion of a liquid under the influence of an applied electric field (potential gradient) relative to a charged solid surface. This electrokinetic phenomenon is a favorable tool to induce flows in microstructures without applying a pressure gradient or the usage of micro-mechanical parts. The utilization of electrokinetic phenomena to improve mixing in micro-flows is described by several authors and, in principle, two different approaches are identified in literature. One approach takes advantage of an electrokinetic instability in which an oscillating electrical potential difference is applied to a layered flow of two liquids with different ionic conductivities.<sup>25,26</sup> This results in a Coulomb force at the liquid-liquid interface which stretches and folds it and mixing of the electrolytes occurs rapidly. A similar effect is observed under the influence of a steady electrical potential difference.<sup>27</sup> The other approach is based on electrokinetic flows of liquids of similar conductivity, whereas the secondary flow regime has to be either created by alternating surface charges (zeta potentials) as shown in Ref. 28 or employing appropriate channel geometries which can be a simple channel T-junction<sup>29</sup> or tips at the channel wall.<sup>30</sup> The mixer concept used in this work relies on the interaction of an electrokinetic and a pressure-driven flow which drives the layered liquids to be mixed through the meander channel. An alternating applied electrical potential gradient induces the oscillating secondary electrokinetic flow, which increases the mixing performance considerably, given a reasonable ratio of main flow to secondary flow amplitudes.<sup>31</sup> This approach is attractive in its simplicity, since it neither relies on specific ionic liquid properties, nor complicated patterning of a microchannel's surface charges. Additionally, the mixing concept does not require complex microfluidic structures and allows for a straightforward control by manipulating the electrical excitation parameter. In our previous work (cf. Ref. 32), a thorough investigation of the electrically excited flow field within the mixer has been carried out. In the present article, we focus on concentration fields and on mixing optimization, since the question of how to operate these mixers is usually not answered, despite the large amount of mixer concepts published in literature. Generally, the control

parameters, which influence the mixing performance are rather intuitively derived. Very few research is concerned with a structured approach including the work of Ansari<sup>33</sup> and Cortes-Quiroz<sup>34</sup> who both report on optimized geometries of the (passive) herringbone mixer.

The present article is organized as follows: At first, a short overview of mixer concept and design is given. We proceed to Sec. III by presenting our 3D mathematical model of the physicochemical processes within the micromixer. This model is implemented in an in-house finite element method (FEM) numerical code which is used to perform simulations of the flow, concentration, and electrical potential field. The model and the numerical schemes are verified by comparison with analogous flow experiments. An extensive discussion of the simulated flow and concentration fields follows. Eventually, the validated simulation code is employed for a numerical optimization of the micromixer in order to achieve high mixing degrees in short operation times. In detail, we optimize the electrokinetic flow by finding the best frequency and amplitude for two forms of electrical excitations, a continuous (sine) and a discrete (square) waveform, and discuss the resulting mixing performances. Finally, this article is summarized with some concluding remarks.

## II. ELECTROKINETIC MICROMIXER

The micromixer geometry under investigation comprises two inlet channels, forming a Y-junction, and a subsequent single meander geometry located downstream in the common outlet channel. The merging channels of the Y-junction feature an angle of 40°. The liquids to be mixed flow through the inlet channels and merge at the Y junction. This base flow is pressure-driven and can be created by employing displacement (syringe) pumps, for instance. Without an applied electrical potential difference, an even, layered flow is observed in the common channel. Here, mixing of the liquids occurs only by diffusion across the (virtual) contact interface of the layered flows. The mixing performance can be considerably improved by applying an alternating potential difference along the microchannel axis, which induces an oscillating electrokinetic flow. The electrokinetic flow creates a secondary velocity component which is, within the bends of the meander channel geometry, perpendicularly directed to the pressure-driven main flow. This secondary velocity component stretches and folds the contact interface of the liquids resulting in higher mixing degrees at the micromixer outlet.

The micromixer concept has been realized for the sake of experimental characterization as described in Ref. 32. The channel geometry is microfabricated by a lithography process in a microfluidic chip made out of Foturan glass and is built of three layers. The base layer is made of Foturan of 1000  $\mu\text{m}$  thickness, with a number of etched holes for inflow and outflow and for accurate relative positioning of the three layers. The mixer layer is made of Foturan of 110  $\mu\text{m}$  thickness in which channels of wideness  $d_0 = 110 \mu\text{m}$  are etched. Consequently, all these flow channels have, to good accuracy, square cross-sections of  $110 \mu\text{m} \times 110 \mu\text{m}$ . Figure 1 gives a schematic drawing of the experimental micromixer setup and mode of operation. The inlet channels and the outlet channel are connected with two inlet reservoirs and an outlet reservoir, respectively, enabling a gravity-driven non-pulsating base flow of small Reynolds numbers. A DC power supply in conjunction with a function generator allows to apply time-dependent potential differences  $\Delta\varphi(t)$  of desired waveform, amplitude, and frequency between the electrodes immersed in the reservoirs. The inlet electrodes are electrically connected, so that the potentials in both inlet reservoirs are identical.

## III. SIMULATION METHODOLOGY

### A. Mathematical formulation of electrical potential, flow, and concentration field

In this section, a brief introduction of a mathematical model capable of describing the physicochemical phenomena within the micromixer is given. The model is based on the method of matched asymptotic expansions (cf. Ref. 35); the detailed derivation of the model is published elsewhere.<sup>32</sup> The model comprises the governing equation of the electrical potential  $\varphi$ , flow field  $(v, u, w)^T$ , pressure  $p$ , and the species concentration  $c_i$ . The equations are related to a

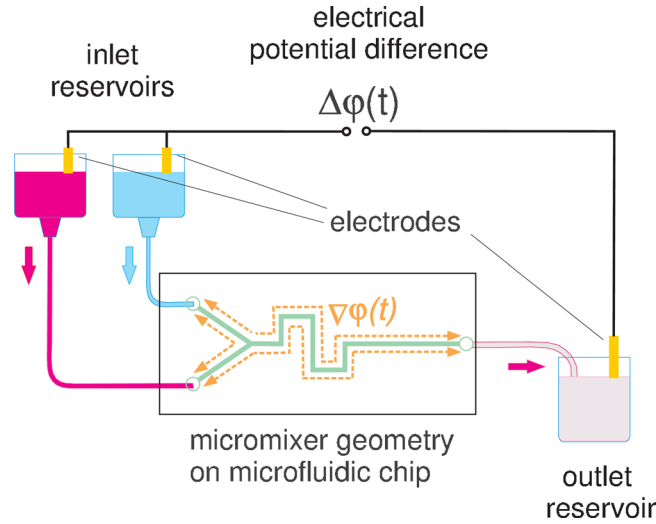


FIG. 1. Sketch of the electrokinetic micromixer principle.

local wall-normal and wall-tangential coordinate system  $(x, y, z)^T$  with the origin at the channel wall. In detail, the model consists of the Poisson-Boltzmann equation, the Navier-Stokes equation extended by a Coulomb force term, and a convection-diffusion species transport equation. All equations are non-dimensionalized with a length scale, a convective velocity scale, a viscous pressure scale, a convective time scale, a potential scale, and a concentration scale; we use

$$\vec{X} = \frac{\vec{x}}{d_0}, \quad \vec{V} = \frac{\vec{v}}{u_0}, \quad P = \frac{pd_0}{\mu u_0}, \quad T = \frac{t}{t_0}, \quad \Phi = \frac{\varphi}{\Delta\varphi_0}, \quad C_i = \frac{c_i}{c_0}. \quad (1)$$

Within the scaling (1),  $d_0$  denotes the channel width,  $u_0$  is the average axial velocity in the common channel,  $t_0 = d_0/u_0$  is a convective time scale,  $\mu$  is the dynamic viscosity,  $\Delta\varphi_0$  is a typical potential difference (e.g., between inlet and outlet electrodes), and  $c_0$  is the initial species concentration. The non-dimensionalization of the governing equations shows two domains, which can be distinguished by whether to or not a Coulomb force acts on the liquid. That is, the electrically neutral bulk liquid and the electrically charged EDL. We find approximate analytical solutions for electrical potential, flow, pressure, and concentration fields within the EDL. These solutions are employed, using the method of matched asymptotic expansions, to infer (transition) boundary conditions for the electrically neutral bulk liquid, which has to be solved numerically. Consequently, a very fine mesh resolution of the EDL, resulting in expensive numerical costs, is omitted.

In detail, in terms of the electrical potential, non-dimensionalization and asymptotic matching lead to a Laplace equation in conjunction with a Neumann boundary condition at the transition between bulk liquid and EDL. That is,

$$\Delta\Phi \simeq 0, \quad (2)$$

$$\frac{\partial\Phi(X, Y, 0)}{\partial Z} \simeq 0. \quad (3)$$

Here, we treat the electrical potential as quasi-instantaneous, since the time for its establishment is much smaller than the convective time scale of the flow  $t_0$ . However, we account for the time-dependency of the electrical potential by introducing a non-dimensionalized excitation frequency corresponding to a Strouhal number

$$St = \frac{fd_0}{u_0} = ft_0, \quad (4)$$

where  $f$  is the dimensional frequency of the electrical potential.

For the flow in the bulk liquid, we obtain the governing equations according to

$$\nabla \cdot \vec{V} = 0, \quad (5)$$

$$Re \left( \frac{\partial \vec{V}}{\partial T} + (\vec{V} \cdot \nabla) \vec{V} \right) = -\nabla P + \Delta \vec{V}, \quad (6)$$

with the corresponding boundary conditions

$$U(T, X, Y, 0) \simeq -\Pi \frac{\partial \Phi}{\partial X}, \quad (7)$$

$$V(T, X, Y, 0) \simeq -\Pi \frac{\partial \Phi}{\partial Y}, \quad (8)$$

$$W(T, X, Y, 0) \simeq 0, \quad (9)$$

$$P(T, X, Y, 0) \simeq C(T, X, Y). \quad (10)$$

Two dimensionless groups arise from non-dimensionalization; the Reynolds number  $Re = \frac{u_0 d_0}{\nu}$  and  $\Pi = \frac{l_D q_\zeta \Delta \phi_0}{u_0 d_0 \mu}$ , which can be interpreted as the ratio of electric to viscous forces. Here,  $\nu$  denotes the kinematic viscosity of the liquid,  $l_D$  is the Debye length, and  $q_\zeta$  is the charge density at the shear layer of the EDL. We see that any wall-tangential electrical potential difference (gradient) leads to a finite velocity transition condition for the bulk solution. The boundary velocity conditions (7) and (8) correspond to the well-known Helmholtz-Smoluchowski slip velocity (cf. Ref. 36). However, there is a distinct difference between both approaches. Smoluchowski essentially neglected the thickness of the EDL and introduced the effect of the EDL by means of the slip velocity while the velocity decrease to zero at the channel wall is not captured. In our approach, the slip velocity appears naturally at the transition between bulk and EDL solution. Hence, the overall solution, which is based on superposition of bulk and asymptotic EDL solutions, captures the velocity decrease and fulfills the no-slip condition at the wall.

The concentration field of species  $i$  is simulated by means of a standard convection-diffusion equation. We arrive after non-dimensionalization in the following governing equation and boundary conditions:

$$\frac{\partial C_i}{\partial T} + \nabla \cdot (\vec{V} C_i) = \frac{1}{Re Sc_i} \Delta C_i, \quad (11)$$

$$\frac{\partial C_i(X, Y, 0)}{\partial Z} = 0. \quad (12)$$

Here,  $Sc_i = \nu/D_i$  is the Schmidt number of dissolved species  $i$ , which is a measure for the ratio of convective to diffusive species transfer rate.

## B. Computational procedure

The mathematical model, discussed in Sec. III A, is implemented in an in-house code HiFlow<sup>3</sup> (www.hiflow3.org) developed by the Engineering Mathematics and Computing Lab (EMCL) at Karlsruhe Institute of Technology (KIT). HiFlow<sup>3</sup> is a multi-purpose finite-element-method toolbox capable for solution of a wide range of physical problems modeled by partial differential equations. Parallel computing—as the foundation for high performance simulations

on modern computing systems—is introduced on two levels: (i) Coarse-grained parallelism by means of distributed grids and distributed data structures; (ii) fine-grained parallelism by means of platform-optimized linear algebra back-ends. Modern numerical schemes in HiFlow<sup>3</sup> are built on top of both levels of parallelism; further information is available in Ref. 37. In the present work, two different high-performance computers are used for the simulations. The first set of micromixer simulations is performed on the distributed memory parallel computer HP XC3000 at Steinbuch Centre for Computing, KIT, Germany equipped with 288 computation nodes. Each node contains two Quad-core Intel Xeon X5540 (2.53 GHz) CPUs and 24 GB of main memory. For the numerical micromixer optimization, we employ the high-performance computer JUROPA-JSC at Forschungszentrum Jülich, Germany equipped with 2208 nodes. Each node is equipped with two Quad-core Intel Xeon X5570 CPUs (2.93 GHz) and 24 GB of main memory.

Despite of these impressive computational resources, we have to limit the computational domain to the meander as shown in Figure 2 in order to obtain reasonable computation times.

This computational domain is “cut out” of the complete micromixer geometry in a distance of five channel widths upstream of the first bend and six and a half channel widths downstream of the last bend, respectively. Note that all dimensions in Figure 2 are scaled by the channel width  $d_0 = 110 \mu\text{m}$ . Due to the fabrication process, we find two different types of corners in the mixer geometry. The radii of the inside and outside corners are 0.41 ( $4.5 \mu\text{m}$ ) and 0.29 ( $3.2 \mu\text{m}$ ), respectively. As the entire microchannel consists of three glass layers, the junction of top and bottom walls to side walls is idealized by right angles. At all boundaries of the computational domain, adequate boundary conditions have to be formulated reflecting the corresponding physics of the complete set-up. According to our mathematical model, the “channel walls” indicate the transition between liquid bulk and EDL.

The model liquids to be mixed are pure water and water with a dissolved tracer. We assume that the tracer does not change the properties of the water, so that all liquid parameters are identical. Density and dynamic viscosity of the liquid are  $\rho = 1000 \text{ kg/m}^3$  and  $10^{-3} \text{ Pa s}$ , respectively. The diffusion coefficient of the tracer is  $D = 4.27 \cdot 10^{-10} \text{ m}^2/\text{s}$ , which gives a Schmidt number of  $Sc = 2340$ . We have to define reasonable initial and boundary conditions for the concentration field, which is not a trivial task. The upstream Y-junction where both liquids meet is not part of the computational domain. We decide to use a rather artificial initial concentration field. At the lower half of the inlet cross-section, we implement a concentration of  $C = 1$ , while at the upper half  $C = 0$  is used. Accordingly, the entire lower and upper half of the microchannels have an initial ( $T = 0$ ) concentration of  $C = 1$  and  $C = 0$ , respectively. A vanishing flux condition  $\partial C / \partial Z = 0$  is engaged at the micromixer outlet and at all transition layers liquid bulk–EDL. To infer appropriate boundary conditions for the electrical potential, we

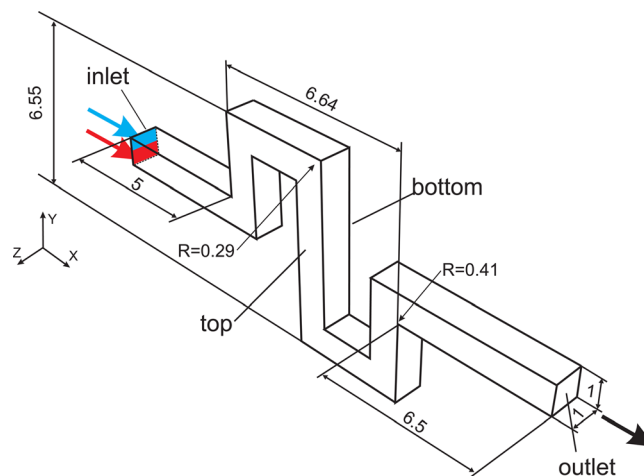


FIG. 2. Sketch of the computational domain.



estimate that 4.7% of the potential difference  $\Delta\varphi$  between inlet and outlet reservoir electrodes drops over the computational domain. Our experiments have typically been performed using potential differences of about 1 kV, so that we choose  $\Delta\varphi_0 = 47$  V as an appropriate scaling parameter for the electrical potential. In principle, the boundary conditions for the potential at the inlet and outlet alternate in time between  $\Phi_{in} \sim 1, \Phi_{out} = 0$  and  $\Phi_{in} = 0, \Phi_{out} \sim 1$ . For the sake of simplification, we permanently set the inlet potential in the computations to be zero and consider only the corresponding outlet potential from now on. At the transition between the liquid bulk solution and the EDL solution,  $\partial\Phi/\partial Z = 0$  is enforced.

To realize the pressure-driven base flow, we implement a tangential body force within the first straight channel part in conjunction with fully developed flow conditions, i.e. ( $\partial U/\partial X = V = W = 0$ ) at the inlet and outlet cross-section (Here,  $X$  and  $U$  are directed downstream along the channel axis). The value of the body force is adjusted to establish the desired Reynolds number in the common channel. Throughout all computations, the velocity and time scales are  $u_0 = 9.1 \cdot 10^{-4}$  m/s and  $t_0 = 0.121$  s, respectively. The electrokinetic flow is introduced into the liquid bulk solution via boundary conditions (7) and (8). Previous experiments have revealed that the charge density at the microchannel wall and the Debye length corresponds to  $q_\zeta = 2.2 \cdot 10^{-3}$  C/m<sup>2</sup> and  $l_D \simeq 216$  nm.<sup>32</sup> Hence we calculate the ratio of electrical to viscous forces to be  $\Pi = 21.36$ , which is used throughout the simulations.

#### IV. FLOW AND CONCENTRATION FIELD

##### A. Flow field

Each mathematical model and its numerical implementation has to be validated to make it a suitable tool for optimization purposes. In this section, we compare three-dimensional (3D) numerical simulations to experimental results obtained with micro particle image velocimetry ( $\mu$ PIV) as described in Ref. 32. In detail, we focus on selected flow fields, which can be found within the lower bends of the micromixer. The Reynolds number of the pressure-driven flow is  $Re = 0.1$ . The electrokinetic flow is excited by an alternating potential difference of  $\Delta\varphi = 1000$  V between the electrodes featuring a square waveform and a frequency of  $f = 0.1$  Hz. Scaling results in a corresponding Strouhal number and an outlet potential amplitude of  $St = 0.012$  and  $\hat{\Phi}_{out} = 1$ , respectively. We observe two different flow regimes within the micromixer depending on the polarity of the electrical potential difference. These flow regimes are, of course, time-dependent. However, within almost the entire half of a wave period, the flow can be considered as (quasi-)steady, since the transition between the flow regimes occurs very quickly. For an outlet potential of  $\Phi_{out} = 1$ , the induced electrokinetic flow is equally directed to the pressure-driven base flow; an even and quasi-steady flow is observed (not shown graphically). The flow regime changes drastically when the electrode polarity changes, i.e.,  $\Phi_{out} = -1$ . The electrokinetic flow is now directed upstream, i.e., against the pressure-driven base flow. This counterflow situation in conjunction with the meander geometry gives rise to highly interesting flow fields, which considerably support mixing. Figure 3 shows selected flow fields by means of particle paths, i.e., we integrate the movement of particles due to the velocity field in planes of constant heights. This method allows us to infer the flow topology in terms of singular points, i.e., vortex and saddle points, and results in a demonstrative illustration of the complex flow regime. The upper row of Figure 3 shows the flow topology measured by  $\mu$ PIV while the lower row displays the results of our numerical simulations.

Figure 3(a) depicts the flow topology at a height level of  $Z = -0.43$ . The measured and simulated pathlines indicate a (quasi-steady) flow from right to left through the meander segment. At this height level close to the bottom wall at  $Z = -0.5$ , the flow field is dominated by the electrokinetic flow.

If we move towards the midplane of the meander segment, the topology of the flow field changes drastically as indicated in Figure 3(b), which shows pathlines at a height level of  $Z = -0.32$ . The measured pathlines are strongly stretched and folded resulting in a complex flow topology, which features various singular points. We find a vortex point (v) and a saddle point (s) in the left (vertical) channel segment, whereas in the right (vertical) channel segment, only a vortex point is found. Another set of vortex and saddle points is observed in the middle

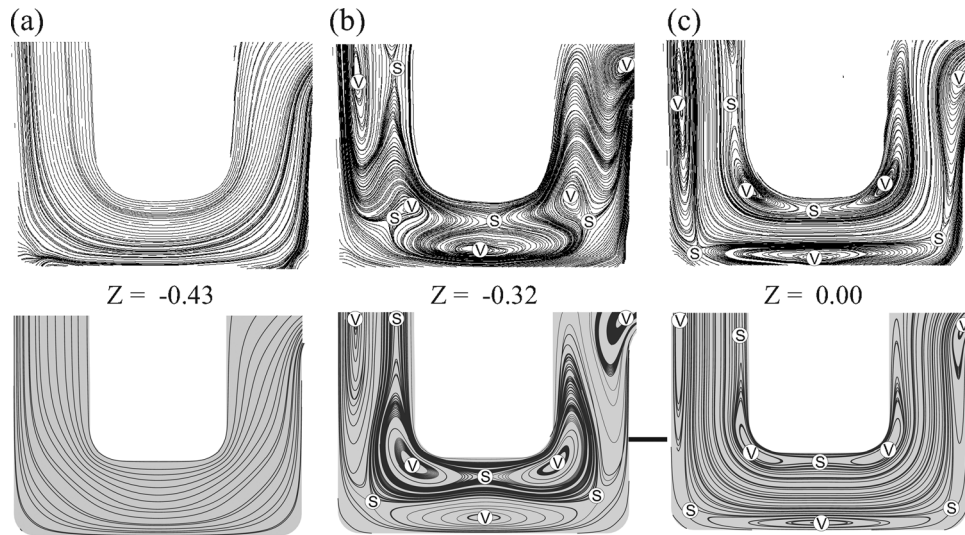


FIG. 3. Measured (upper row) and simulated (lower row) path lines in the flow at constant height levels (a)  $Z = -0.43$ , (b)  $Z = -0.32$ , and (c)  $Z = 0.00$ . The flow consists of a pressure-driven base flow with  $Re = 0.1$  and a counter-directed electrokinetic flow.

(horizontal) channel segment. Furthermore, we find a pair of saddle and vortex points within each bend. This complex flow field results from the mutual influence of the electrokinetic and pressure-driven flows present close to all channel walls and within the channel core, respectively. If we compare measured and simulated pathlines, the overall picture is in a very good agreement. All singular points are rediscovered featuring an equal type and almost identical positions. Likewise, the characteristics of the pathlines appear similar within the channel segment.

The flow topology in the mid-height level ( $Z = 0$ ) of the meander segment is presented in Figure 3(c). The measured pathlines reveal a quasi-steady and even flow, from left to right, which is the pressure-driven part of the flow located within the centre of the microchannel. Adjacent to the walls, the electrokinetic part of the flow is counter-directed from right to left giving rise to several singular points located at the (shear) interface between the two flows. In detail, we rediscover all singular points known from height level  $Z = -0.32$ , whereas some positions are slightly changed. For instance, saddle and vortex points previously located in the bend centers are moved towards the bend corners. The comparison between measured and simulated pathlines shows again a very good agreement with respect to type and position of the singular points and the pathlines characteristics.

The present results reveal some further interesting aspects when we refer to our previous work<sup>32</sup> where we compared measured and simulated pathlines obtained with a different numerical code, which cannot be employed for optimization purposes, and, more importantly, with a simplified numerical mesh structure. The simplified mesh consisted of a perfect rectangular geometry featuring sharp edges and corners, which cannot be achieved in reality due to constraints imposed by microfabrication processes, e.g., by etching. The simplified mesh simulations showed several distinct topology differences. Within the inner (protruding) corner of the bends, we previously obtained two vortices and a separating saddle. In contrast, the present results show a single vortex and a separating saddle in both experimental and simulation results. We concluded that the difference is due to the sharp edges/corners; an assumption which is verified by the simulations in this work performed with an improved and much more expensive mesh corresponding to a more realistic micromixer geometry.

To summarize, the comparison of measured and simulated results proves that the numerical code HiFlow<sup>3</sup> is able to reproduce the complex flow fields in the electrokinetic micromixer with an excellent agreement. This validation of the mathematical models and their numerical



implementations with respect to the flow field serves as a basis for further simulations of the concentration fields and, eventually, for the electrokinetic optimization.

## B. Concentration field

We now focus on different concentration fields, which are present in the micromixer as a result of different (non-optimized) electrical excitations. We only present results of numerical simulations, since the measurement of complex, time-dependent 3D concentration fields in microchannels is a rather difficult task. In a previous work,<sup>38</sup> we have engaged micro laser-induced fluorescence ( $\mu$ LIF) method to investigate the influence of Dean vortices, induced by a pure pressure-driven flow of  $Re \cong 20..40$ , on the concentration field within the meandering microchannel geometry. In contrast to the application of fluorescence intensity techniques to macroscopic flows (LIF), this method illuminates the complete microchannel volume. This results in height-averaged concentration fields, which can be easily misinterpreted. In principle, if a LIF method is coupled with a scanning confocal microscope, as shown in Ref. 39 for mixing in slug flows, measurements of 3D concentration fields in microstructures are possible. However, even for microchannels, the scanning across the channel height takes a relatively long time. Thus, this method is restricted to steady concentration fields or to concentration fields with a regular recurrence of patterns, so that the measurements can be synchronized.

Figure 4 shows the concentration field within the midplane of the micromixer for different modes of electrical excitation. The Reynolds and Schmidt numbers are  $Re = 1$  and  $Sc = 2340$ ,

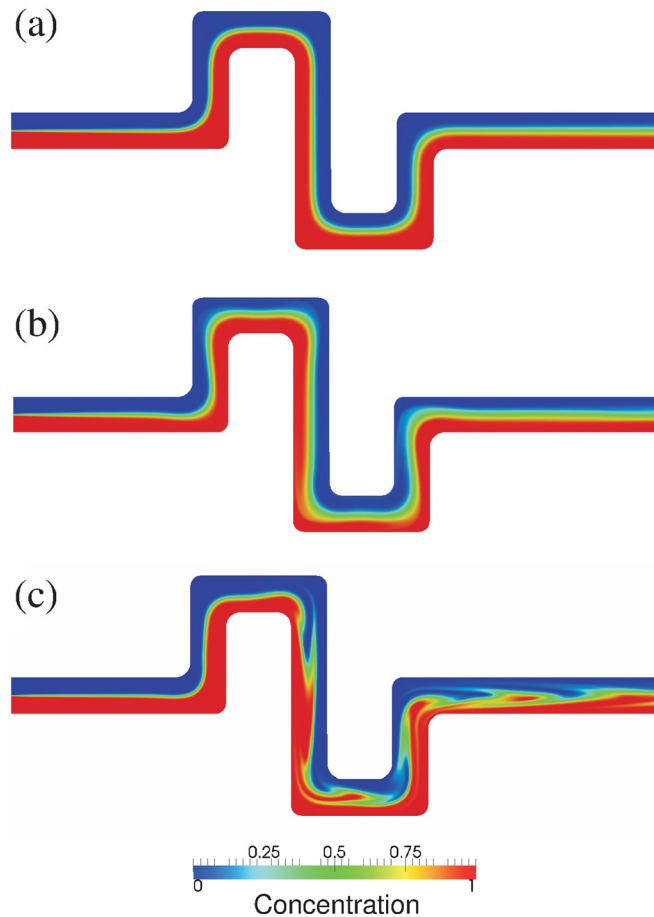


FIG. 4. 3D simulations of the concentration field within the midplane of the micromixer at  $T = 30$  for different modes of electrical excitations: (a) pure pressure-driven flow; (b) pressure-driven flow with a steady counter-directed electrokinetic flow; and (c) pressure-driven flow and an alternating electrokinetic flow ( $\Phi_{out} = 1$  and  $St = 0.1$ ). The Reynolds and Schmidt numbers are  $Re = 1$  and  $Sc = 2340$ , respectively.

respectively, the simulation time is restricted to  $T=30$ , since we are interested in achieving good mixing results in short times. Figure 4(a) shows the concentration field for a pure pressure-driven flow without any electrical excitation corresponding to a Strouhal Number of  $St=0$ . We basically recognize three layers of liquid. The lower (red) layer is at tracer concentrations around  $C=1$  and the upper (blue) layer is at concentrations around  $C=0$ . Further, a thin (green) concentration boundary layer of mixed liquid ( $C=0.5$ ) is present between the upper and the lower layer. In the absence of electrical excitation, it can be clearly seen that mixing occurs only by diffusion across the contact interface of both (blue and red) liquids. The thickness of this concentration boundary layer increases along the channel axis as the residence time of the liquids increases.

Figure 4(b) shows the concentration field as a result of a constant electrical potential  $\Phi_{out} = 1$ , which can be interpreted as a wave signal of infinite high frequency, i.e.,  $St \rightarrow \infty$ . The electrical potential induces an electrokinetic flow, which is counter-directed to the pressure-driven base flow. Comparable to Figure 4(a), we find an even concentration field characterized by three liquid layers. In contrast to Figure 4(a), however, it can be seen that the concentration boundary layer between blue and red liquid is wider. This implies that a higher fraction of mixed liquid leaves the mixer outlet compared to the pure pressure-driven flow regime. This can be simply explained by the residence time. The counter-directed electrokinetic flow decreases the total flow rate. Hence, the residence time of the liquids within the mixer geometry is increased, and there is more time for diffusive mixing across the contact interface.

The concentration field for the micromixer operated with a time-dependent electrical excitation is given by Figure 4(c). Here, the outlet electrical potential has a square waveform, an amplitude of  $\hat{\Phi}_{out} = 1$  and alternates with an arbitrarily chosen frequency of  $St=0.1$ . We find several locations where the concentration boundary layer is folded and stretched which increases the contact interface area and, consequently, facilitates mixing by diffusion. The stretching and folding is induced by the interaction of the meandering geometry and the alternating electrokinetic flow. The electrokinetic flow is perpendicular-directed to the pressure-driven base flow within the bends. This secondary flow transports liquid by convection across the channel center into locations previously occupied by the other liquid. Additionally, the flow regime switches between an even flow and the flow fields illustrated in Figure 3. The complex flow topologies close to the channel walls as a result of mutual influence of pressure-driven and (counter-directed) electrokinetic flow contribute to mixing as well. Even though the performance might be better than for the previous operation modes, it is obvious that the mixer does not operate at its best. The electrical excitation settings used here are an educated guess. Eventually, all shown concentration fields demonstrate the need for an systematic optimization of the micromixer's mode of operation.

## V. OPTIMIZATION

In this section, we employ the validated numerical tools to optimize the mixing performance of the electrokinetic micromixer. Even though we have access to considerable computational resources, in terms of optimization, we have to further restrict simulations. The dimensionless tracer diffusion coefficient of our mixing problem ( $Re=1$ ,  $Sc=2340$ ) is given as  $D=1/(Re Sc)$ . This value in conjunction with the cell Peclet number  $Pe_c = UL/D$  allows to infer a roughly suitable mesh size  $L$  for our computations. Given a mean velocity of  $U \simeq 1$  and the necessary condition that  $Pe \lesssim 1$ , the maximal size of a mesh cell should be  $L \lesssim 1/2340 \approx 0.0004 (0.05 \mu\text{m})$ . A 3D optimization with such a fine mesh is far beyond the computational capabilities accessible for this work. Hence, we concentrate on 2D optimizations and restrict the computations to the midplane ( $Z=0$ ) of the micromixer. This simplification is justified after inspecting the concentration fields of the micromixer at different height levels as can be seen in Ref. 40. Even though the flow topology changes considerably along the channel height (cf. Figure 3), the concentration fields are similar. Likewise, a comparison of midplane flow and concentration fields obtained from 3D and 2D simulations reveals a very good qualitative agreement.

In general, we have to identify the common features of a optimization problem prior to the application optimization techniques.<sup>41</sup> That is: (i) A quantitative criterion that has to be optimized, which is usually formulated as a cost functional; (ii) One or more control or design parameters that can be modified to achieve an optimization; (iii) And finally, the constraints which have to be fulfilled within the optimization problem.

A simple approach to express perfect mixing of two liquids is to correlate it to a respective concentration  $C_M$ . In the case of two identical liquids with ( $C = 1$ ) and without tracer ( $C = 0$ ), perfect mixing is given for a concentration of  $C_M = 0.5$ . A practical, quantitative mixing criterion can be achieved by integrating the quadratic difference from perfect mixing in an area of interest  $\Omega_s$  for each time step. Hence, the cost functional for the optimization is defined to be

$$J(C, T) \equiv \int_{\Omega_s} (C(T) - C_M)^2 d\vec{X}. \quad (13)$$

We consider the last horizontal channel segment of the meander as the area of interest  $\Omega_s$ . Eventually, perfect mixing is achieved when the cost functional  $J(C, T)$  is zero.

The performance of the micromixer can be effectively influenced by different control/design parameters. These include geometric factors, such as number of bends or length ratio of horizontal to vertical channel segments, and flow parameters, such as the Reynolds number, which can be adjusted more easily. In this work, we restrict the optimization efforts to the secondary electrokinetic flow, which can be conveniently manipulated in form of the electrical excitation (control) parameters  $\alpha_k$  including outlet potential's amplitude  $\hat{\Phi}$ , frequency (Strouhal number  $St$ ), and waveform. In detail, we perform optimizations for two different outlet potentials featuring a discrete and a continuous waveform. The first optimization is performed using a discrete square wave potential. We choose a Fourier series approximation for the sake of differentiability, i.e.,

$$\Phi_{out,1}(T, \alpha_k) = \frac{4\hat{\Phi}_1}{\pi} \sum_{j=0}^n \frac{\sin((2j-1)2\pi St_1 T)}{2j-1}. \quad (14)$$

Practically, we limit the number of Fourier terms to  $n = 10$ . The second optimization is performed for a continuous outlet potential of sinusoidal waveform. We have

$$\Phi_{out,2}(T, \alpha_k) = \Phi_2 + \hat{\Phi}_2 \sin(2\pi St_2 T), \quad (15)$$

with the potential offset  $\Phi_2$  as additional control parameter. The constraints within our optimization problem are specified by the mathematical model and the corresponding boundary conditions as described in Sec. III. In terms of practical applications, rapid mixing is also a desirable feature and we, therefore, restrict the time interval to be  $T \in [0, 30]$ .

Common optimization methods can principally be distinguished by the determination of the cost functional gradient. Two approaches are common, the adjoint- and the sensitivity-based approach. Both approaches calculate the gradient of the cost functional with respect to the control parameter to solve the optimization problem. For a time dependent problem, the adjoint-based approach requires forward- and backward-in-time solutions of the adjoint equations while sensitivity-based methods only project forward in time. That is, the adjoint-based approach determines  $\nabla J(C, \alpha_k)$  simultaneously and independent of the number of parameters  $\alpha_k$ , whereas the sensitivity-based approach requires the solution of a linearized problem for each  $\alpha_k$ . In this work, we use a sensitivity-based approach, whereas the chain rule is applied to derive the gradient of the cost functional (13). Eventually, the optimization problem of the electrokinetic micromixer can be formulated as

$$\min_{C, \alpha_k} J(C, \alpha_k) \equiv \frac{1}{2} \int_0^T \int_{\Omega_s} (C(T) - C_M)^2 d\vec{X} dT + \frac{\lambda}{2} \sum_{k=1}^m |\alpha_k|^2, \quad (16)$$

whereas  $\lambda$  is the regularization term, which can be chosen to control the optimization problem and  $m$  is the number of control parameters of the optimization problem. Further information on the sensitivity-based optimization methods used in our work can be found in Refs. 41–44.

We solve the optimization problem for a flow of  $Re = 1$  and two different electrical excitations  $\Phi_{out,1}, \Phi_{out,2}$ , so that the mathematical model, boundary conditions, and Eq. (16) are fulfilled. The resulting optimized control parameters for both waveforms are given in Table I. The optimization of the discrete (square waveform) outlet potential  $\Phi_{out,1}$  indicates best mixing for an amplitude and frequency of  $\hat{\Phi}_1 = 1.490$  and  $St_1 = 0.208$ , respectively. Regarding the continuous (sine waveform) electrical excitation, the optimization shows no need for an offset of the potential. The optimal amplitude and frequency are  $\hat{\Phi}_2 = 1.476$  and  $St = 0.210$ , respectively. Surprisingly, there is practically no difference between the continuous and the discrete electrical excitation signals but the waveform. Moreover, the optimal Strouhal number is relatively small, since everyone would intuitively assume that the mixing performance increases with the excitation frequency.

To obtain further insight into the nature of these optimization values, we review some typical time scales of our problem. The (dimensionless) mean residence time in the mixer  $T_r$  can be estimated by the ratio of dimensionless straight mixer length  $L_0 = 23$  and the average dimensionless flow velocity  $U = 1$ ; we obtain  $T_r \cong L_0/U \approx 23$ . Using Eq. (7), we calculate that the electrokinetic flow amplitude for the optimized operation corresponds to  $U_{EOF} \cong 1/10U$ . The convective time scale of the electrokinetic flow is given by the ratio of channel diameter to electrokinetic velocity; it is  $T_{EOF} \cong 1/U_{EOF} \approx 10$ . We conclude that good mixing is achieved when the convective time scale of the electrokinetic flow is similar to the mean residence time in the mixer.

Additionally, the comparison of viscous and excitation time scales gives further information on the optimization results. Electrokinetic flow occurs in the very thin EDL, and the adjacent bulk liquid is dragged by viscous forces only. Every excitation which is (much) faster than the viscous time scale is damped by inertia and remains without effect. We introduce the Reynolds number of our electrically excited flow  $Re_f = d_0^2 f / \nu$  as the ratio of viscous time scale to excitation time scale (also inertial force/viscous force). The electrokinetic flow will follow the excitation as long as inertia has no significant influence; i.e., for  $Re_f \ll 1$ , which will only occur if the excitation frequencies are on the order of or smaller than  $St \lesssim 0.1$  ( $f \lesssim 10$  Hz). A comparison of this limit shows good agreement to the optimized Strouhal number of  $St \approx 0.2$ . Presumably, the optimized frequency is the practical upper limit for the current flow configuration, and any further increase is without effect.

We plot the evolution of the cost functional (degree of mixing) vs. the simulation time for different electrical excitation modes in Figure 5 to obtain a better insight into the mixing performance. In detail, we plot the cost functionals  $J(C, T)$ , scaled with the (initial) cost functional at  $T = 0$ , for the pure pressure-driven flow, for the non-optimized square wave potential as discussed in Sec. IV B, and for the optimized square and sine waveform potentials. The pure pressure-driven flow (solid line) without any electrical excitation indicates the baseline for all cases. We see that starting from a value of 1, the scaled cost functional decreases to about 0.7 at  $T \approx 15$  and then slowly approaches a steady value of about 0.74 for  $T \gtrsim 23$ . The steady value is solely related to the concentration boundary layer between the two layered liquids and is the minimum degree of diffusive mixing, which can be achieved for the given geometry and (layered) flow. The time which is required to achieve the steady cost functional corresponds to the mean residence time. We define a diffusive mixing time  $T_m \equiv T_r = L_m^2 Re Sc$ , whereas  $L_m$  is a

TABLE I. Optimized control parameters for two different electrical excitations.

Excitation	Offset	Amplitude	Frequency
square wave potential $\Phi_{out,1}$	–	$\hat{\Phi}_1 = 1.490$	$St_1 = 0.208$
sine wave potential $\Phi_{out,2}$	$\Phi_2 = 0.018$	$\hat{\Phi}_2 = 1.476$	$St_2 = 0.210$

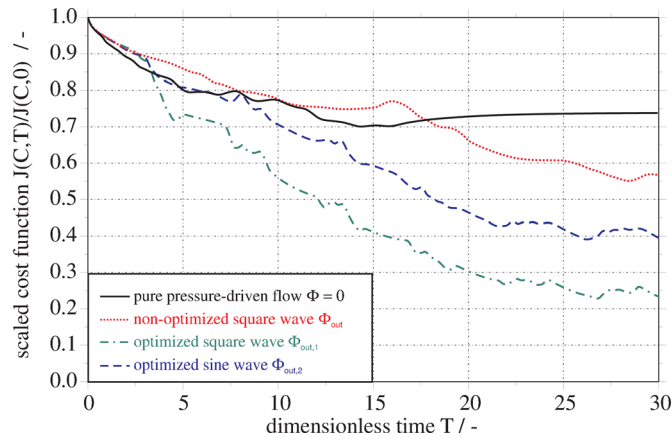


FIG. 5. Evolution of the cost functional, scaled with the (initial) value at  $T=0$ , vs. the dimensionless simulation time  $T$  for different modes of electrical excitation.

diffusive mixing length, which corresponds to the distance by which species  $i$  transversely diffuses into the unmixed liquid. The diffusive mixing length is estimated according to  $L_m = \sqrt{\frac{T_m}{ReSc}} \approx 0.1$ . Consequently, the tracer's maximum diffusion path, which indicates the diffusive mixing contribution, is on the order of 1/10 of the channel diameter for the given Reynolds number. Theoretically, this value cannot be increased for a given residence time and further mixing increase has to be achieved by enlargement of the contact interface between the layered flows.

The mixer operated with the non-optimized square wave potential  $\Phi_{out}(\hat{\Phi} = 1, St = 0.1)$  (dotted line) achieves a value of about 0.57 at  $T=30$  (cf. Figure 4(c)). This represents a performance improvement compared to the mixer with the pure pressure-driven flow even though the electrical excitation setting was arbitrarily chosen. When the micromixer is operated with the optimized potentials, higher mixing degrees in shorter mixing times are generally achieved compared to the previous cases. The mixer excited with the sine wave potential  $\Phi_{out,2}$  (dashed line) approaches a final value of 0.4, whereas the operation with the square wave potential  $\Phi_{out,1}$  (dashed-dotted line) results in 0.23 at  $T=30$ . Eventually, even though amplitude and frequency of both optimized potentials are similar, the performance of the mixer operated with the discrete signal is distinctively superior to the mixer operated with the continuous signal.

In order to give an illustrative visualization of the computed cost functionals, we discuss the corresponding concentration fields, whereas the results of the pure pressure-driven case and the non-optimized electrical excitation have been already given in Figures 4(a) and 4(c). Figure 6 shows the evolution of the concentration fields for an electrokinetic flow excited by the optimized sine wave potential  $\Phi_{out,2}$  at (a)  $T=10$ , (b)  $T=20$ , and (c)  $T=30$  of the optimization interval. At  $T=10$ , we find a smooth concentration boundary layer between the liquids in the first part of the meander geometry. In the second part, the boundary layer is considerably folded and stretched providing a higher exchange area for diffusive mixing. However, the concentration boundary layer is still relatively thin, since there has not been sufficient time for diffusive mixing ( $T < T_m$ ). At  $T=20$ , the concentration boundary layer shape is principally similar but wider compared to the previous time. This operation time corresponds approximately to the diffusive mixing time ( $T \approx T_m$ ). Even though a considerable fraction of  $\Omega_s$  is occupied by mixed liquid, the concentration field appears somewhat heterogenous. If we increase the simulation time to  $T=30$ , the shape and thickness of the concentration boundary layer appears similar to the previously discussed operation time. Eventually, we observe that the flow field induces an optimal concentration boundary layer structure early ( $T \lesssim 10$ ) as indicated by the similar shapes of the concentration boundary layer at all inspected times. All further mixing is based on diffusive processes, which are limited by the diffusive mixing time scale ( $T_m \cong 20$ ). An



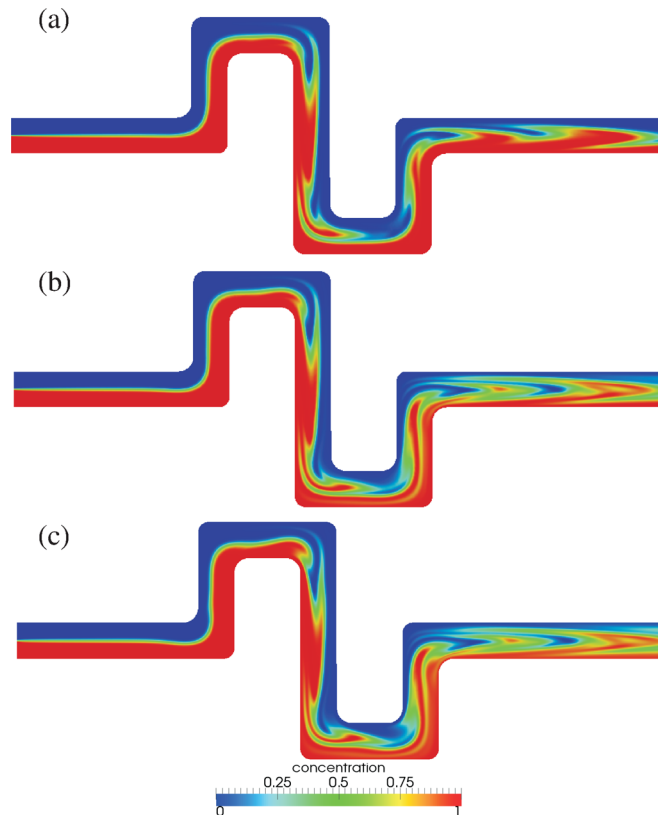


FIG. 6. Concentration fields in the midplane of the micromixer at (a)  $T = 10$ , (b)  $T = 20$ , and (c)  $T = 30$ . The flow consists of a pressure-driven base flow with  $Re = 1$  and an optimized electrokinetic flow induced by the optimized sine wave potential  $\Phi_{out,2}$ .

operation time exceeding  $T > T_m$  has only minor influence on the overall mixing degree. Further (local) diffusive mixing improvements are only possible in the small layers close to the channel walls where the fluid elements have residence times higher than the diffusive mixing time scale.

The concentration fields in the mixer when operated with the optimized square wave potential  $\Phi_{out,1}$  are given in Figure 7 for (a)  $T = 10$ , (b)  $T = 20$ , and (c)  $T = 30$  of the optimization interval. We find improved mixing results for all operation times compared to the sine wave excitation as already indicated by the generally lower scaled cost functionals. At  $T \geq T_m$ , the domain  $\Omega_s$  is mainly filled with mixed liquid, whereas some minor unmixed areas are present as well. Again, the difference in the electrical excitation resulting in the optimized concentration fields plotted in Figures 6 and 7 is just the waveform. A comparison shows similar concentration patterns for both excitations; obviously a result of the equal amplitudes and frequencies. However, it appears that the discrete potential results in a more pronounced stretching and folding of the contact interface. This is presumably related to the duration of the velocity amplitude of the secondary flow. The square wave potential induces a maximum electrokinetic velocity, which is present over the entire half of the wave period. The electrokinetic velocity as a result of the sine wave potential, however, increases continuously from zero to the maximum value over one quarter of the period and immediately decreases again. Consequently, there is less convective transport of liquid across the channel center towards the other liquid when operated with the continuous signal.

Eventually, we would like to critically compare our work with the methods of Jain and Nandakumar<sup>45</sup> who introduced a novel comparative mixing index (CMI) for micromixer characterization and comparison. Mixing improvements are often achieved at the expense of reduced flow rates. The CMI accounts for varying residence times and compares the mixing improvement to

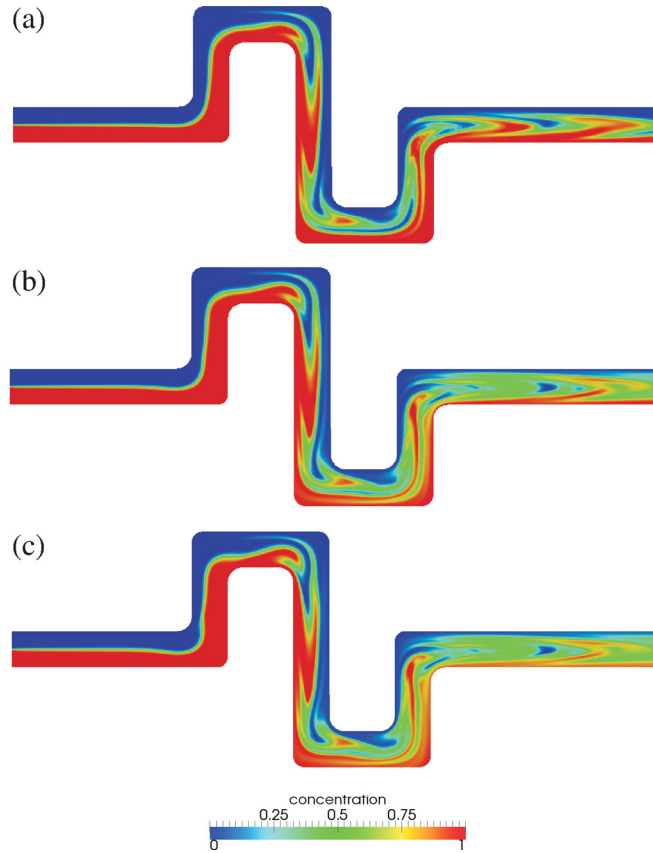


FIG. 7. Concentration fields in the midplane of the micromixer at (a)  $T = 10$ , (b)  $T = 20$ , and (c)  $T = 30$ . The flow consists of a pressure-driven base flow with  $Re = 1$  and an optimized electrokinetic flow induced by the optimized square wave potential  $\Phi_{out,1}$ .

pure transverse (diffusive) mixing in a layered flow as it occurs in a simple T-mixer and, of course, in our mixer when operated without electrical excitation. In the present work, we apply the CMI to compare the different operation modes, whereas some adjustments have to be made. First, we do not have to account for different residence times, since they are approximately constant for all investigated cases. This is due to periodicity and small amplitudes of the electrokinetic flow, which hardly contribute to the (time-averaged) flow rates. Second, Jain and Nandakumar compare different mixer designs, all based on flows of two layered liquids, with the T-Mixer. The aim of the present work is the comparison of different modes of operation in one mixer design. Nevertheless, since our micromixer is also based on a layered flow, we employ a modified CMI, which compares mixing degrees of an electrically excited mixer to the pure pressure-driven flow mixer (baseline). We rewrite the cost functional, so that we obtain a mixing degree  $\eta_m(T)$ , which is zero and one for total unmixed and total mixed state, respectively. Furthermore, we would like to expand the idea of Jain and Nandakumar that mixing of layered flows scales with the (dimensionless) transverse diffusive flux  $\dot{N}_i$  of species  $i$  integrated over the (straight) channel length. If mixing improvement is mainly achieved by folding of the contact interface between the liquids, the mixing degree scales with  $\dot{N}_i$  integrated over the length of the (folded) concentration boundary layer  $L_c$ . Hence, we can write

$$\eta_m(T) = 1 - \frac{J_m(C, T)}{J_m(C, 0)} \propto \int_0^{L_c} \dot{N}_i d\vec{X} \sim \frac{\Delta C_i}{ReSc_i} L_c. \quad (17)$$

The CMI can then be defined as the ratio of the mixing degrees of electrically excited mixer and pure pressure-driven flow mixer

TABLE II. Mixer efficiency  $\eta_m$  and comparative mixer index  $\alpha_{m,0}$  at simulation time  $T=30$ .

Mode of operation $m$	$\eta_m(30)$	$\alpha_{m,0}(30)$
pure pressure-driven flow $\Phi_{out} = 0$	0.26	1
non-optimized square wave potential $\Phi_{out}$	0.43	1.65
optimized sine wave potential $\Phi_{out,1}$	0.60	2.31
optimized square wave potential $\Phi_{out,2}$	0.77	2.93

$$\alpha_{m,0}(T) = \frac{\eta_m(T)}{\eta_0(T)} \sim \frac{L_c}{L_0}, \quad (18)$$

which can also be interpreted as the ratio of folded concentration boundary layer length  $L_c$  due to electrical excitation to the concentration boundary layer length of the even-layered flow, i.e., the straight mixer length  $L_0$ . Table II summarizes mixing degrees  $\eta_m$  and mixing improvement  $\alpha_{m,0}$  compared to the pure-pressure driven flow for different excitation modes. We obtain mixing improvements up to about 300% when the mixer is optimally operated. This CMI is considerably higher than the mixer designs investigated by Jain and Nandakumar. However, a direct comparison of the mixer efficiencies is difficult, since their mixers are operated at lower Reynolds numbers and higher Schmidt numbers.

## VI. CONCLUDING REMARKS

In this article, we undertake investigations on the optimization of an electrokinetic micro-mixer. The electrokinetic flow is induced by an alternating electrical potential difference applied between the mixer's in- and outlet. Suitable modes of electrical excitation to achieve good mixing results, i.e., amplitude, frequency, and waveform of the applied potential difference, are not known and respective technical/design guidelines do not exist.

We, therefore, implement a mathematical model of the electrical potential, flow, and concentration field into a FEM code. Model and numerical implementations are validated against experimental observations of the complex flow topology present in the lower channel segment of the micromixer geometry. The corresponding concentration fields clarify that, even though an increased mixing performance is observed when the mixer is electrically excited, the mixer does not operate at its best. Hence, there is a need to optimize the mode of operation, which can be done by engaging our validated numerical model in conjunction with adequate numerical optimization strategies.

We restrict the optimization efforts to the electrokinetic flow, which can be conveniently controlled in form of the electrical excitation parameters potential amplitude, frequency (Strouhal number), and waveform. Two exemplary waveforms are chosen, a square wave and a sine wave potential representing a discrete and a continuous excitation. It turns out that the optimized amplitudes and frequency for both electrical excitation modes are almost identical. Generally, the optimized outlet electrical potentials induce a (secondary) electrokinetic flow amplitude, which is about 1/10 of the pressure-driven main flow amplitude. For this ratio, the convective time scale of the electrokinetic flow roughly corresponds to the mean residence time of the mixer. The optimal dimensional frequency of  $St \cong 0.2$  ( $f \cong 15$  Hz) is presumably an upper limit, which can be achieved before the electrical excitation is damped by inertial effects. A further noteworthy observation of the present optimization results is the influence of the waveform. A considerable superior mixing performance is observed for the discrete over the continuous excitation, even though amplitudes and frequencies are similar.

In summary, the present work demonstrates that the electrokinetic mixing concept is able to achieve high mixing degrees in short operation times, given a reasonable ratio of main flow to secondary flow amplitudes and an appropriate excitation frequency. It is understood that the mixer concept works only in a certain range of Reynolds numbers. In theory, we will have perfect mixing for layered flows of  $Re \rightarrow 0$  without any electrical excitation, and we will have no

mixing at all for  $Re \rightarrow \infty$  independent of the excitation. For finite Reynolds numbers, the frequency and amplitude of the electrical excitation have to be adjusted accordingly, whereas several limitations exist. In practice, only electrokinetic velocity amplitudes on the order of  $\hat{u}_{EOF,max} \sim 10$  mm/s can be achieved due to nonlinear effects such as joule heating. If we assume that for flows of  $Re > 1$ , the optimum ratio of electrokinetic to pressure-driven velocity amplitude is still around 1/10, we estimate that the electrokinetic mixer works for pressure-driven flows of up to  $Re \lesssim 10$ , i.e., for the majority of lab-on-a-chip applications, given that the time scale of the required excitation frequency is sufficiently larger than the viscous time scale to exclude considerable damping due to inertia. The question whether to or not other discrete, continuous, harmonic, or disharmonic electrical excitation waveforms exist, which result in improved mixing degrees at shorter times must be answered in future work. An optimization with a completely arbitrary electrical potential, using the adjoint-based optimization approach, is desirable, but this would require even more expensive computations.

Finally, the practical applicability of the present mixer concept should be discussed with respect to electrochemical reactions, which occur at the electrodes. On one hand, the relatively low frequency and the high electrical potential difference may oxidize/reduce the sample/species to be mixed and eventually change its concentrations. On the other hand, the mixer operation inevitably results in electrolytic dissociation of water generating (dissolved) gases (hydrogen, oxygen), which might influence the pH value as well. Nevertheless, these problems should only be critical if the ratio of electrode areas to liquid volume is relatively large as it may occur for designs having internal planar electrodes located at opposite microchannel walls. Most microfluidic chips, however, have a design comprising wire electrodes, having very small surface areas, which are immersed in large sample and waste reservoirs. Since electrochemical conversion scales directly with the electrode area, the resulting very small conversion rates should neither influence concentrations nor produce enough gases that the solubility limits are exceeded even for times much longer than typical operation/mixer times. In case such microfluidic designs are not available, several chemical means could be engaged as well. Suitable buffers would mitigate the problem of pH changes. Additionally, suitable reagents having low redox potentials could be added, which are electrochemically converted instead of the sample/species or the water, whereas the condition is that the reaction products have no negative impacts on the system. Eventually, our mixer concept shares the same difficulties as all designs based on electrokinetic flows. It should not be employed if the sample is sensitive to stresses arising from high electric fields as it may be the case for viable organisms such as viruses or bacteria.

<sup>1</sup>H. A. Stone, A. D. Stroock, and A. Ajdari, "Engineering flows in small devices: Microfluidics toward a lab-on-a-chip," *Annu. Rev. Fluid Mech.* **36**, 381–411 (2004).

<sup>2</sup>T. M. Squires and S. R. Quake, "Microfluidics: Fluid physics at the nanoliter scale," *Rev. Mod. Phys.* **77**, 977–1026 (2005).

<sup>3</sup>P. Nghe, E. Terriac, M. Schneider, Z. Z. Li, M. Cloitre, P. Abecassisa, and B. Tabeling, "Microfluidics and complex fluids," *Lab Chip* **11**, 788–794 (2011).

<sup>4</sup>E. Kamio, T. Ono, and H. Yoshizawa, "Design of a new static micromixer having simple structure and excellent mixing performance," *Lab Chip* **9**, 1809–1812 (2009).

<sup>5</sup>Y.-C. Lin, Y.-C. Chung, and C.-Y. Wu, "Mixing enhancement of the passive microfluidic mixer with j-shaped baffles in the tee channel," *Biomed. Microdevices* **9**, 215–221 (2007).

<sup>6</sup>Y. Yamaguchi, F. Takagi, K. Yamashita, H. Nakamura, H. Maeda, K. Sotowa, K. Kusakabe, Y. Yamasaki, and S. Morooska, "3-d simulation and visualization of laminar flow in a microchannel with hair-pin curves," *AIChE J.* **50**, 1530–1535 (2004).

<sup>7</sup>L. Chen, G. Wang, C. Lim, G. H. Seong, J. Choo, E. K. Lee, S. H. Kang, and J. M. Song, "Evaluation of passive mixing behaviors in a pillar obstruction poly(dimethylsiloxane) microfluidic mixer using fluorescence microscopy," *Microfluid. Nanofluid.* **7**, 267–273 (2009).

<sup>8</sup>J. Melin, G. Giménez, N. Roxhed, W. van der Wijngaart, and G. Stemme, "A fast passive and planar liquid sample micromixer," *Lab Chip* **4**, 214–219 (2004).

<sup>9</sup>R.-T. Tsai and C.-Y. Wu, "An efficient micromixer based on multidirectional vortices due to baffles and channel curvature," *Biomicrofluidics* **5**, 014103 (2011).

<sup>10</sup>A. D. Stroock, S. K. W. Dertinger, A. Ajdari, I. Mezić, H. A. Stone, and G. M. Whitesides, "Chaotic mixer for microchannels," *Science* **295**, 647–651 (2002).

<sup>11</sup>Y. Du, Z. Zhang, C. H. Yim, M. Lin, and X. Cao, "A simplified design of the staggered herringbone micromixer for practical applications," *Biomicrofluidics* **4**, 024105 (2010).

<sup>12</sup>Y. C. Lam, H. Y. Gan, N. T. Nguyen, and H. Lie, "Micromixer based on viscoelastic flow instability at low Reynolds number," *Biomicrofluidics* **3**, 014106 (2009).

- <sup>13</sup>V. Hessel, S. Hardt, H. Löwe, and F. Schönfeld, "Laminar mixing in different interdigital micromixers: I. Experimental characterization," *AIChE J.* **49**, 566–577 (2003).
- <sup>14</sup>D. Ahmed, X. Mao, J. Shi, B. K. Juluri, and T. J. Huang, "A fast microfluidic mixer based on acoustically driven sidewall-trapped microbubbles," *Microfluid. Nanofluid.* **7**, 727–731 (2009).
- <sup>15</sup>P. D. Khatavkar, V. V. Anderson, J. M. J. den Toonder, and H. E. H. Meijer, "Active micromixer based on artificial cilia," *Phys. Fluids* **19**, 083605 (2007).
- <sup>16</sup>M. Yi, S. Qian, and H. H. Bau, "A magnetohydrodynamic chaotic stirrer," *J. Fluid Mech.* **468**, 153–177 (2002).
- <sup>17</sup>S. Oberti, A. Neild, and T. W. Ng, "Microfluidic mixing under low frequency vibration," *Lab Chip* **9**, 1435–1438 (2009).
- <sup>18</sup>D. J. Laser and J. G. Santiago, "A review of micropumps," *J. Micromech. Microeng.* **14**, R35–R64 (2004).
- <sup>19</sup>P. Wang, Z. Chen, and H.-C. Chang, "A new electro-osmotic pump based on silica monoliths," *Sens. Actuators B* **113**, 500–509 (2006).
- <sup>20</sup>D. P. J. Barz and P. Ehrhard, "Model and verification of electrokinetic flow and transport in a micro electrophoresis device," *Lab Chip* **5**, 949–958 (2005).
- <sup>21</sup>A. R. Minerick, A. E. Ostafin, and H.-C. Chang, "Electrokinetic transport of red blood cells," *Electrophoresis* **23**, 2165–2173 (2002).
- <sup>22</sup>J. Voldman, "Electrical forces for microscale cell manipulation," *Annu. Rev. Biomed. Eng.* **8**, 425–454 (2006).
- <sup>23</sup>Y. Kang and D. Li, "Electrokinetic motion of particles and cells in microchannels," *Microfluid. Nanofluid.* **6**, 431–460 (2009).
- <sup>24</sup>A. V. Delgado, F. Gonzalez-Caballero, R. J. Hunter, L. K. Koopal, and J. Lyklema, "Measurement and interpretation of electrokinetic phenomena," *J. Colloid Interface Sci.* **309**, 194–224 (2007).
- <sup>25</sup>M. H. Oddy, J. G. Santiago, and J. C. Mikkelsen, "Electrokinetic instability micromixing," *Anal. Chem.* **73**, 5822–5832 (2001).
- <sup>26</sup>C.-C. Chen, H. Lin, S. K. Lele, and J. G. Santiago, "Convective and absolute electrokinetic instability with conductivity gradients," *J. Fluid Mech.* **524**, 263–303 (2005).
- <sup>27</sup>A. O. E. Moctar, N. Aubry, and J. Batton, "Electrohydrodynamic microfluidic mixer," *Lab Chip* **3**, 273–280 (2003).
- <sup>28</sup>D. Erickson and D. Li, "Microchannel flow with patchwise and periodic surface heterogeneity," *Langmuir* **18**, 8949–8959 (2002).
- <sup>29</sup>C. Y. Lim, Y. C. Lam, and C. Yang, "Mixing enhancement in microfluidic channel with a constriction under periodic electro-osmotic flow," *Biomicrofluidics* **4**, 014101 (2010).
- <sup>30</sup>J.-K. Chen and R.-J. Yang, "Vortex generation in electroosmotic flow passing through sharp corners," *Microfluid. Nanofluid.* **5**, 719–725 (2008).
- <sup>31</sup>I. Meisel and P. Ehrhard, "Electrically excited (electroosmotic) flows in microchannels for mixing applications," *Eur. J. Mech. B/Fluids* **25**, 491–504 (2006).
- <sup>32</sup>D. P. J. Barz, H. F. Zadeh, and P. Ehrhard, "Flow fields within an electrokinetic micromixer," *J. Fluid Mech.* **676**, 265–293 (2011).
- <sup>33</sup>M. A. Ansari and K.-Y. Kim, "Shape optimization of a micromixer with staggered herringbone groove," *Chem. Eng. Sci.* **62**, 6687–6695 (2007).
- <sup>34</sup>C. A. Cortes-Quiroz, M. Zangeneh, and A. Goto, "On multi-objective optimization of geometry of staggered herringbone micromixer," *Microfluid. Nanofluid.* **7**, 29–43 (2009).
- <sup>35</sup>M. van Dyke, *Perturbation Methods in Fluid Mechanics* (The Parabolic Press, Stanford, 1975).
- <sup>36</sup>M. v. Smoluchowski, "Contribution à la théorie de l'endosmose électrique et de quelques phénomènes corrélatifs," *Bull. Int. Acad. Sci. Cracovie* **8**, 182–200 (1903).
- <sup>37</sup>H. Anzt, W. Augustin, M. Baumann, H. Bockelmann, T. Gengenbach, T. Hahn, V. Heuveline, E. Ketelaer, D. Lukarski, A. Otzen, S. Ritterbusch, B. Rucker, S. Ronnas, M. Schick, C. Subramanian, J.-P. Weiss, and F. Wilhelm, "HiFlow<sup>3</sup> - A flexible and hardware-aware parallel finite element package," Tech. Rep. No. 2010-06, Preprint Series of the Engineering Mathematics and Computing Lab (EMCL)—Karlsruhe Institute of Technology, 2010.
- <sup>38</sup>D. P. J. Barz, H. F. Zadeh, and P. Ehrhard, "Laminar flow and mass transport in a twice-folded microchannel," *AIChE J.* **54**, 381–393 (2008).
- <sup>39</sup>A. Guenther, M. Jhunjhunwala, M. Thalmann, M. A. Schmidt, and K. F. Jensen, "Micromixing of miscible liquids in segmented gas-liquid flow," *Langmuir* **21**, 1547–1555 (2005).
- <sup>40</sup>H. Bockelmann, *High Performance Computing Based Methods for Simulation and Optimisation of Flow Problems*, Ph.D. thesis, Fakultät für Mathematik, Universität Karlsruhe, 2010.
- <sup>41</sup>M. D. Gunzburger, *Perspectives in Flow Control and Optimization* (SIAM, 2003).
- <sup>42</sup>M. D. Gunzburger, "Adjoint equation-based methods for control problems in incompressible, viscous flows," *Flow, Turbul. Combust.* **65**, 249–272 (2000).
- <sup>43</sup>K. Kunisch, *Optimal Control of Coupled Systems of Partial Differential Equations, International Series of Numerical Mathematics*, edited by G. Leugering, J. Sprekels, and F. Tröltzsch (Birkhaeuser Basel, Basel, 2009).
- <sup>44</sup>F. Tröltzsch, *Optimal Control of Partial Differential Equations: Theory, Methods and Applications, Graduate studies in mathematics Vol. 112* (American Mathematical Society, Providence, RI, 2010).
- <sup>45</sup>M. Jain and K. Nandakumar, "Novel index for micromixing characterization and comparative analysis," *Biomicrofluidics* **4**, 031101 (2010).